



# Uncertainty quantification of MEMS using a data-dependent adaptive stochastic collocation method

Aravind Alwan, N.R. Aluru\*

Department of Mechanical Science and Engineering, Beckman Institute for Advanced Science and Technology, University of Illinois at Urbana-Champaign, 405 N. Mathews Avenue, Urbana, IL 61801, United States

## ARTICLE INFO

### Article history:

Received 23 December 2010  
Received in revised form 22 June 2011  
Accepted 23 June 2011  
Available online 1 July 2011

### Keywords:

Uncertainty quantification  
Hybrid electrothermomechanical (ETM) actuation  
Microelectromechanical systems (MEMS)  
Stochastic collocation  
Adaptive analysis

## ABSTRACT

This paper presents a unified framework for uncertainty quantification (UQ) in microelectromechanical systems (MEMS). The goal is to model uncertainties in the input parameters of micromechanical devices and to quantify their effect on the final performance of the device. We consider different electromechanical actuators that operate using a combination of electrostatic and electrothermal modes of actuation, for which high-fidelity numerical models have been developed. We use a data-driven framework to generate stochastic models based on experimentally observed uncertainties in geometric and material parameters. Since we are primarily interested in quantifying the statistics of the output parameters of interest, we develop an adaptive refinement strategy to efficiently propagate the uncertainty through the device model, in order to obtain quantities like the mean and the variance of the stochastic solution with minimal computational effort. We demonstrate the efficacy of this framework by performing UQ in some examples of electrostatic and electrothermomechanical microactuators. We also validate the method by comparing our results with experimentally determined uncertainties in an electrostatic microswitch. We show how our framework results in the accurate computation of uncertainties in micromechanical systems with lower computational effort.

© 2011 Elsevier B.V. All rights reserved.

## 1. Introduction

Uncertainty quantification has become an important component in the design of most engineering systems and is widely used to predict the performance of a device, given a random manufacturing or operating environment. It is especially important in areas like micromachining, where manufacturing tolerances are much worse than what one might design for. Micromechanical devices are typically fashioned on wafers, with each wafer supporting anywhere from a few hundred to a few thousand devices. Ideally, the design of a typical microelectromechanical system (MEMS) must be robust enough to tolerate deviations in fabrication processes not only from one wafer to the next, but also spatially across a single wafer. However, due to practical limitations, it is not always possible to tightly control tolerances and this results in very different behavior, going from one device to the next. Although several advances have been made in the development of high-fidelity numerical methods to model microsystems [1–6], there is a pressing need to augment the capability of these methods to handle the uncertainties that are encountered in a realistic device model. In some cases, the undesirable effects caused by certain uncertainties can be mitigated by overcompensating other parameters, e.g. by

increasing the voltage applied on an RF-MEM switch, one can ensure that pull-in will occur even in the presence of variations in the mechanical stiffness of the switch electrodes. However, this practice results in poor, inefficient designs and may even affect the lifetime of the device, e.g. the lifetime of an RF-MEM switch is shown to decrease exponentially with the voltage applied across it [7], due to phenomena like dielectric charging. In this paper, we develop a framework to accurately quantify the effect of uncertainties in MEMS in order to improve the design of such devices. A first step towards tackling this problem is to increase our understanding of the random processes at play by modeling the uncertainty and accurately calculating its statistics of interest.

In order to perform uncertainty analysis in MEMS, we face two important challenges. The first challenge is to identify and model the sources of uncertainty that affect a device of our interest. For most systems, the nature of uncertainty in the input parameters is usually unknown and is approximated using some standard distribution [8]. However, in the case of parameters encountered in micromechanical devices, it may not always be possible to describe the uncertainty using a standard distribution. Agarwal and Aluru [9] proposed a data-driven framework that generates a probability distribution for input parameters by estimating the uncertainty using actual experimental data. A data-driven framework does not place any assumptions on the nature of uncertainty and is extensible to any device parameter for which sufficient experimental data is available.

\* Corresponding author.

E-mail address: [aluru@illinois.edu](mailto:aluru@illinois.edu) (N.R. Aluru).

URL: <http://www.illinois.edu/~aluru> (N.R. Aluru).

The second challenge is to propagate the stochastic model through the system to understand how the uncertainties propagate into output quantities of interest. Traditionally, the engineering answer to this problem is to construct an elaborate *design of experiments* (DOE) that sufficiently replicates the gamut of variations that might typically be encountered. However, in the case of micro-mechanical devices, such an approach might turn out to be quite expensive in terms of time and effort. For particular types of uncertainty, it may not even be possible to come up with a comprehensive DOE procedure that captures the randomness with sufficient accuracy. With the advent of numerical solvers that accurately model complex multiphysics phenomena in devices, it is now possible to replicate the DOE on a computer without compromising on the accuracy in the results. There are many methods available in the literature, that are tailored towards performing this uncertainty quantification efficiently. Sampling-based methods like the Monte Carlo method have been used as the basis for implementing reliability-based design optimization techniques [10–12] to achieve robust designs in microsystems. Recently, there has also been a focus on non-statistical methods based on the Galerkin formulation, such that those that employ wavelet-based basis functions [13,14] and generalized polynomial chaos [8,15,16]. Stochastic collocation [17,18] is another method that has recently gained popularity. This method uses the idea of collocation, where the stochastic solution is approximated by interpolating the values of the solution obtained at specific collocation points in the parameter space. Modifications of this method have been suggested, where adaptive refinement of the collocation grid [19,20] is used to reduce the computational cost of constructing the interpolant. To perform UQ in realistic MEM devices, it is important to keep in mind that the particular method that we employ should also be flexible enough to accommodate any arbitrary stochastic model that is generated by the data-driven framework. It is also highly desirable to be able to propagate the uncertainty with minimal computational effort.

The goal of this paper is to present a unified framework for the quantification of uncertainty in MEMS. We are mainly interested in quantifying uncertainties by means of their statistical parameters, e.g. mean, variance, etc., which are the quantities that are most useful from a practical designer's point of view. Hence, we shall limit our focus to methods that perform the task of estimating these statistics efficiently with minimal computational effort, while maintaining accuracy. Our goal is to develop a generic model to describe uncertainties commonly encountered in microsystems and to quantify the effect of these uncertainties on device performance.

The paper is organized as follows: Section 2 describes the physical models governing the behaviour of the microactuator devices that we consider. These models are used to numerically simulate the device in order to perform uncertainty quantification. Section 3 then examines the sources of randomness in these devices and explains the generation of stochastic models that describe these uncertainties. It also introduces several methods for the propagation of these uncertainties through the device model, which are used to characterize the variation in output parameters of interest. In this context, it argues for the use of methods for the efficient estimation of statistics of the stochastic solution. All these methods are applied for the quantification of uncertainty in a few example micromechanical devices described in Section 4. We consider electromechanical actuators and describe how variations in their geometrical or material parameters affect their behaviour. Section 5 presents the concluding remarks.

## 2. Physical level modeling

We perform uncertainty quantification on the general class of electrothermomechanical (ETM) microactuators, which convert

electrical energy to mechanical force or displacement. Based on the actuation mechanism, most of these actuators can be classified as either electrostatic actuators or electrothermal actuators. Recently, it has been shown that these two modes of actuation can also be integrated in a single device [21]. This hybrid ETM device operates with greater efficiency, producing larger displacements using the same operational voltage. Furthermore, it can be shown that the hybrid ETM model describes a more general class of devices, of which electrothermal and electrostatic actuators are special cases. We choose this model for demonstrating UQ due to the highly coupled interaction between electrical, thermal and mechanical fields, making it an ideal device for studying the propagation of uncertainties.

### 2.1. Hybrid ETM actuators

Hybrid ETM actuators integrate electrostatic and electrothermal modes of actuation in a single device. A typical device comprises a movable electrode placed next to a fixed ground plate, as shown in Fig. 1. The movable electrode has a double beam shape similar to a bent-beam electrothermal microactuator and is equipped with two electrical terminals. Potential differences may be applied across the terminals of the movable electrode as well as between the terminals of the movable and fixed electrodes. This results in the flow of current within the movable electrode, which causes Joule heating and consequently, electrothermal expansion. Due to the characteristic shape of this electrode, the constrained expansion forces it to bend towards the fixed electrode. The potential difference between the fixed and moving electrodes also creates an electrostatic field between them and corresponding electrostatic traction on the boundaries. Using a combination of these two forces, it is possible to achieve a larger displacement for the same applied potential difference than that obtained in similar actuators that employ either pure electrostatic or electrothermal actuation. In this section, we describe a physical model that governs the displacement of the actuator in terms of the device parameters. We present only a brief outline of the model here; a more complete description of the model is given in [21].

We model the problem using the two dimensional domain as shown in Fig. 1. In order to solve for the displacement in the actuator, we need to obtain a self-consistent solution between the coupled mechanical, thermal and electrical fields in the problem domain. Since we are interested in the steady-state behaviour of the device, we ignore all transient effects and seek the equilibrium solution of these fields. We also note that the mechanical displacement in the movable electrode causes the problem domain to deform and necessitates that the equations be expressed and solved in the deformed configuration for accurate results. This can be easily achieved by transforming all the equations from the deformed configuration to the undeformed reference domain (denoted by  $\Omega_1$ ,  $\Omega_2$  and  $\bar{\Omega}$ ) corresponding to the initial state. This mapping is adequately described by the deformation gradient,  $\mathbf{F}$ , in the

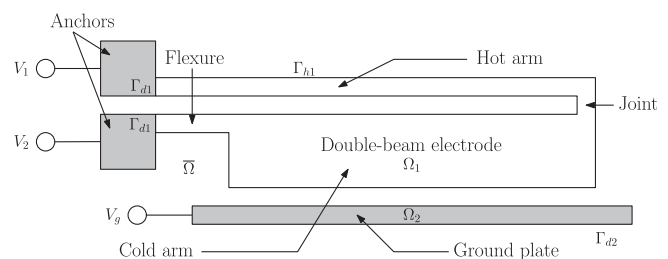


Fig. 1. Problem domain used to model a typical hybrid ETM actuator.

domain. Using such a Lagrangian formulation, we can directly solve the equations in the reference configuration.

We first describe the mechanical deformation of the actuator by means of a 2D geometrically nonlinear formulation. Since the ground plate is held fixed, we need to only solve for the mechanical displacement in the double-beam electrode. Denoting the displacement vector field by  $\mathbf{u}$  and the deformation gradient by  $\mathbf{F} = \mathbf{I} + \nabla \mathbf{u}$ ,  $\mathbf{I}$  being the identity tensor, the mechanical deformation of the double-beam electrode is given by [22],

$$\nabla \cdot (\mathbf{FS}) = 0 \quad \text{in } \Omega_1, \quad (1)$$

$$\mathbf{u} = 0 \quad \text{on } \Gamma_{d1}, \quad (2)$$

$$\mathbf{PN} = \mathbf{H} \quad \text{on } \Gamma_{h1}, \quad (3)$$

where  $\Gamma_{d1}$  is the part of the movable electrode boundary where a Dirichlet boundary condition is applied,  $\mathbf{P}$  is the first Piola–Kirchhoff stress tensor,  $\mathbf{N}$  is the unit outward normal vector in the reference configuration and  $\mathbf{H}$  is the surface traction vector that describes the electrostatic traction acting on the interfaces. Eq. (3) is the electrostatic traction boundary condition, which is applied on the rest of the boundary  $\Gamma_{h1}$ .  $\mathbf{S}$  is the second Piola–Kirchhoff stress tensor given by [23]

$$\mathbf{S} = \mathbf{CE}_s - \frac{Y\alpha}{1-\nu} \Delta \mathbf{I}, \quad (4)$$

where  $\mathbf{C}$  is the material tensor,  $\mathbf{E}_s$  is the Green–Lagrangian strain tensor,  $Y$  is the Young’s modulus,  $\alpha$  is the coefficient of thermal expansion,  $\nu$  is the Poisson’s ratio and  $\mathbf{I}$  is the identity tensor. We define a reference temperature,  $T_0$ , at which thermal strains are assumed to be zero, and denote  $\Delta T = T - T_0$  as the deviation of the current temperature,  $T$ , from this reference. We see that Eq. (4) describes the electrothermal coupling through the thermal strains that develop in the actuator due to Joule heating.

To obtain the temperature profile that causes the thermal expansion, we prescribe a heat source in the double-beam electrode and assign appropriate boundary conditions by constraining the temperature on  $\Gamma_{d1}$  to the reference temperature  $T_0$  and allowing for convective heat transfer on the side walls as well as on the top and bottom surfaces of the device. The temperature field,  $T$ , is obtained by solving the heat conduction equation expressed in the reference configuration [23,24],

$$\nabla \cdot (\mathbf{JF}^{-1} \mathbf{q}_t) = Q - \frac{h_{tb}}{t} (T - T_\infty) \quad \text{in } \Omega_1, \quad (5)$$

$$T = T_0 \quad \text{on } \Gamma_{d1}, \quad (6)$$

$$\mathbf{JF}^{-1} \mathbf{q}_t \cdot \mathbf{N} = h_s (T - T_\infty) \quad \text{on } \Gamma_{h1}, \quad (7)$$

where  $J = \det \mathbf{F}$  is the Jacobian of the deformation gradient and  $\mathbf{q}_t = -k_t \mathbf{F}^{-T} \nabla T$  is the heat flux in the body, where  $k_t$  is the uniform, isotropic value of thermal conductivity for the material. The heat supply per unit volume due to resistive Joule heating is denoted by  $Q$  and is computed from the potential field,  $\phi$ , as

$$Q = k_e \nabla \phi \cdot \nabla \phi, \quad (8)$$

where  $k_e$  is the uniform, isotropic value of electrical conductivity for the material. The convective heat transfer from free surfaces is described by the terms containing  $h_{tb}$  and  $h_s$  in Eqs. (5) and (7).  $h_{tb}$  corresponds to the coefficients of convective heat transfer from the top and bottom surfaces, while  $h_s$  applies to the side walls of the body. The thickness of the device in the direction perpendicular to the plane of the problem domain is denoted by  $t$ , while  $T_\infty$  is the ambient temperature far away from the body and  $\mathbf{N}$  is the unit outward normal vector on the boundary.

Finally, we need to solve for the electrical field that is responsible for the electrostatic traction as well as the Joule heating. The design of the hybrid ETM actuator is such that the movable electrode is made of an isotropic material with a finite value of electrical

conductivity, which admits a non-zero electric field within it. This field causes the flow of current within the double-beam electrode, which in turn causes the Joule heating as described above. In addition, an electric field is also created in the medium surrounding the electrodes.

To solve for the electric potential in the entire region, we first assign a small fictitious value of electrical conductivity to the surrounding dielectric medium. The ground plate is assumed to be metallic and its boundary can be regarded as an equipotential surface. We then model the electrical problem using the current conduction equation [25] by considering the entire domain as a region with a piecewise homogeneous value of conductivity. Dirichlet boundary conditions are applied by prescribing the potential at the anchored boundaries of the double-beam electrode ( $\Gamma_{d1}$ ) and the entire boundary of the ground plate ( $\Gamma_{d2}$ ). We also impose the continuity of potential and normal current density at the interface between the movable electrode and the dielectric medium ( $\Gamma_{h1}$ ). The system of equations that describe the electric potential  $\phi$  are:

$$\nabla \cdot (\mathbf{JF}^{-1} k_{e1} \mathbf{F}^{-T} \nabla \phi) = 0 \quad \text{in } \Omega_1, \quad (9)$$

$$\nabla \cdot (\mathbf{JF}^{-1} k_{e0} \mathbf{F}^{-T} \nabla \phi) = 0 \quad \text{in } \bar{\Omega}, \quad (10)$$

$$\phi = \phi_0 \quad \text{on } \Gamma_d, \quad (11)$$

$$\phi|_{\Omega_1} = \phi|_{\bar{\Omega}} \quad \text{on } \Gamma_{h1}, \quad (12)$$

$$[\mathbf{JF}^{-1} k_{e1} \mathbf{F}^{-T} \nabla \phi \cdot \mathbf{N}]_{\Omega_1} = [\mathbf{JF}^{-1} k_{e0} \mathbf{F}^{-T} \nabla \phi \cdot \mathbf{N}]_{\bar{\Omega}} \quad \text{on } \Gamma_{h1}, \quad (13)$$

where  $\phi_0$  is the prescribed potential, while  $k_{e1}$  and  $k_{e0}$  denote the electrical conductivities of the top electrode and the exterior region, respectively.  $\Gamma_d = \Gamma_{d1} \cup \Gamma_{d2}$  denotes the portion of the boundary where the Dirichlet boundary condition is applied.

We complete the mathematical description of the problem, by computing the electrostatic traction term  $\mathbf{H}$  on the electrode surfaces. The electrostatic traction in the reference configuration can now be computed as,

$$\mathbf{H} = J |\mathbf{F}^{-T} \mathbf{N}| \mathbf{f}_{es}, \quad (14)$$

where  $\mathbf{f}_{es}$  is the electrostatic traction in the deformed configuration. This traction depends on the surface charge density,  $\sigma_s$ , that develops on all interfaces where there is discontinuity in either the electrical conductivity or dielectric permittivity. Denoting the normal current density as  $J_n$  and the dielectric permittivity as  $\epsilon$ , we can express the surface charge density and electrostatic traction at any general interface in the deformed configuration as [25]:

$$\sigma_s = J_n \left[ \frac{\epsilon}{k_e} \Big|_+ - \frac{\epsilon}{k_e} \Big|_- \right], \quad (15)$$

$$\mathbf{f}_{es} = \frac{1}{2} \sigma_s \{ (E_n|_- + E_n|_+) \mathbf{n} + 2E_t|_- \mathbf{t} \}, \quad (16)$$

where  $E_n$  and  $E_t$  are the components of the electric field,  $\mathbf{E} = -\nabla \phi$ , along the unit normal and tangential vectors in the deformed configuration,  $\mathbf{n}$  and  $\mathbf{t}$ , respectively. Since the normal current density is continuous across the interface, the normal component of the electric field on either side of the interface can be related to the current density through Ohm’s law,  $J_n = k_e|_- E_n|_- = k_e|_+ E_n|_+$ . If we assume that the unit normal vector,  $\mathbf{n}$ , is pointed outward with respect to the double-beam electrode, then the  $-$  sign refers to the conducting material that makes up the electrode and the  $+$  sign refers to the dielectric medium surrounding it.

One important point to note is that Eq. (10) describes the variation of electric potential in the dielectric medium surrounding the electrodes, denoted by  $\bar{\Omega}$ . Since the extent of  $\bar{\Omega}$  is infinite, it is convenient to use a boundary integral formulation [26,27], to efficiently solve this equation. The details of this formulation are given in [21]. Using this boundary integral formulation, we solve

for the coupled thermal, electrical and mechanical fields in a self-consistent manner to obtain the final solution.

## 2.2. Electrostatic microswitches

Electrostatic actuators are currently the most commonly used mode of actuation in microelectromechanical switches. They can be represented as a special case of hybrid ETM model described above. A typical device consists of a movable electrode, usually a beam clamped at one or both ends, held parallel to a fixed ground plate (Fig. 2). Both electrodes usually have very high values of conductivity and can be effectively modeled as being metallic. A potential difference is applied between the movable electrode and the fixed one, creating an electric field in the region between them and consequently, an electrostatic force on the movable electrode.

We again seek the steady-state potential and displacement fields in the two dimensional problem domain shown in Fig. 2. The mechanical displacement is governed by the same system of equations (Eqs. (1)–(3)) as in the hybrid ETM case. The only difference is that in the absence of electrothermal expansion, the second Piola–Kirchhoff stress tensor reduces to the usual form of the constitutive relationship,

$$\mathbf{S} = \mathbf{C}\mathbf{E}_s. \quad (17)$$

Due to the additional assumption that the movable electrode is also metallic, we no longer need to solve for the electric potential inside the electrode, since the electric field is zero within it. This means that the entire boundary of the movable electrode can be considered as an equipotential surface. The system of equations describing the electric potential, reduces to just solving the Laplace equation in the dielectric medium surrounding the electrodes, with Dirichlet boundary conditions on all the electrode boundaries.

$$\nabla \cdot (\mathbf{J}\mathbf{F}^{-1}\mathbf{F}^{-T}\nabla\phi) = 0 \quad \text{in } \bar{\Omega}, \quad (18)$$

$$\phi = \phi_0 \quad \text{on } \Gamma_d, \Gamma_{h1}. \quad (19)$$

Under the assumption of the electrodes being modeled as metallic, the surface charge density and the electrostatic traction at the metal–dielectric interface can be obtained from the usual expressions for  $\sigma_s$  and  $\mathbf{f}_{es}$  in terms of the normal electric field, as  $\sigma_s = \epsilon E_n$  and  $\mathbf{f}_{es} = [\sigma_s^2/(2\epsilon)]\mathbf{n}$ , where  $\epsilon$  is the dielectric permittivity of the surrounding medium. By plugging these expressions into Eq. (14), we obtain the electrostatic traction in the reference configuration, which can be used to solve for the mechanical displacement. We solve for the coupled electrical and mechanical fields successively until we converge to a self-consistent solution.

## 3. Stochastic analysis

In the previous section, we described the physical model and the set of equations that govern the hybrid ETM actuator. Typically, we construct such a model to obtain the relationship between a few output parameters of interest like displacement of the actuator

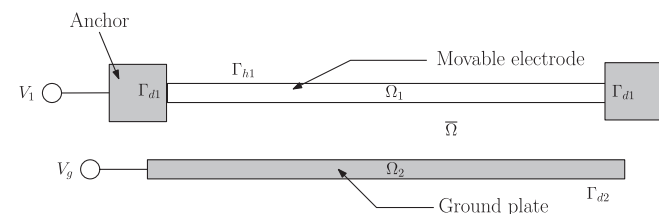


Fig. 2. Problem domain used to model a typical electrostatic actuator that uses a fixed–fixed beam as the movable electrode.

tip, actuation force, etc. and a number of input parameters like device dimensions and properties of the materials that make up the device. For example, in the case of the hybrid ETM actuator, we observe that the actuator displacement depends on the device dimensions like actuator length, inter-electrode gap, etc. as well as the material properties like thermal conductivity and elastic modulus of the material comprising the double-beam electrode. In a real device, several of these parameters could have large uncertainties and can vary quite significantly from one device to the next. This would cause a significant deviation in device behaviour from that predicted by the model using only one set of parameters. To obtain a better picture of the actuator performance, it is important to perform a stochastic analysis, where we model the uncertainties in the inputs and propagate these uncertainties through the system to predict the variation in output quantities of interest.

### 3.1. Generating a stochastic model

In order to quantify variation in the device behaviour it is important to have an accurate model for the uncertainty in the inputs. In the context of MEMS, this translates into developing a stochastic model for device-specific input parameters. In most cases, the only available information regarding the uncertainty is a set of measurements obtained from device characterization experiments. As a first approximation, it may be possible to assume that uncertain quantities follow some known standard distribution function, e.g. that the values are uniformly distributed in some interval or that they are normally distributed about some mean value. This forms the basis of parametric estimation, where we first assume that the data belongs to a certain class of distribution functions and then try to estimate the parameters of the distribution to obtain a close match to the data. However, in the absence of any physical justification for such an assumption, it may be incorrect to try to empirically fit some standard distribution to the given data.

#### 3.1.1. Non-parametric density estimation

Non-parametric density estimation is a better alternative, as it does not make any assumptions about the nature of randomness in the data; rather the model structure is determined from the data. Although this class of methods employs models that use parameters, they are *distribution-free* in the sense that the number and type of parameters are not assumed *a priori*. As a result, this method is robust and in most cases, it can accurately model the underlying distribution in the data. A typical example is kernel density estimation (KDE) [28]. KDE estimates the probability density function (PDF) at any point as a sum of contributions from kernel functions centered at the data points. The kernels provide a smoothed value for the density at points lying in between the data points. The optimal PDF is chosen corresponding to a specific bandwidth of the kernels that optimizes some risk function, which ensures that the estimated density approaches the actual one in the asymptotic limit of having an infinite sample of data. Given a data set  $\{x_1, x_2, \dots, x_M\}$ , we can use KDE to construct an estimate  $\hat{\rho}(x)$  of the unknown PDF  $\rho(x)$  as,

$$\hat{\rho}(x) = \frac{1}{M\beta} \sum_{i=1}^M K\left(\frac{x - x_i}{\beta}\right), \quad (20)$$

where  $K(z)$  is the kernel function,  $\beta$  is the kernel bandwidth and  $M$  is the number of observations that are available. A popularly used kernel is the Gaussian kernel with unit variance centered at zero,

$$K(x) = \frac{1}{\sqrt{2\pi}} e^{-x^2/2}. \quad (21)$$

It is interesting to note that the form of the estimated density obtained through KDE based on the Gaussian kernel is similar to the solution of the heat diffusion equation initialized with point sources. This analogy between KDE and the heat diffusion equation [29] motivates the formulation of a diffusion-mixing-based estimator [30]. The estimated density obtained using this method is given by [9],

$$\hat{\rho}(x, t) = \frac{1}{M\sqrt{2\pi t}} \sum_{i=1}^M e^{-(x-x_i)^2/2t}, \quad (22)$$

where the square root of the diffusion or mixing time,  $\sqrt{t}$ , is analogous to the bandwidth in the case of KDE and is chosen in a similar fashion. In situations where some prior information regarding the density function is available, it is useful to incorporate this into the density estimation process, to obtain an estimate that is close to the prior density. This can be done by extending the diffusion model into a more general method by considering the generalized heat diffusion equation [30],

$$\frac{\partial}{\partial t} \hat{\rho}(x, t) = \frac{1}{2} \frac{\partial}{\partial x} \left( a(x) \frac{\partial}{\partial x} \left( \frac{\hat{\rho}(x, t)}{p(x)} \right) \right), \quad x \in \mathcal{D}, \quad t > 0, \quad (23)$$

where  $p(x)$  is the probability density function that represents the prior information that is available and  $a(x)$  is a positive function chosen in the computational domain  $\mathcal{D}$ . The computational domain is chosen such that it contains the given data and is large enough to assume the boundary condition that the estimated density goes to zero on its boundary, i.e.  $\hat{\rho}(x, t) = 0$  on the boundary of  $\mathcal{D}$ . The additional terms,  $a(x)$  and  $p(x)$ , result in variable drift and diffusivity and can be used to achieve smoothing of the density in regions where data is sparse and sharpening in regions of high concentrations of data. As in the case of the standard diffusion-based estimator, we set the initial conditions for this PDE using the empirical density obtained by placing point sources at the data-points,

$$\hat{\rho}(x, 0) = \frac{1}{M} \sum_{i=1}^M \delta(x - x_i). \quad (24)$$

If prior information is available in the form of a density function,  $p(x)$ , then it can be directly used in Eq. (23) to obtain a density estimate. When such a prior density is not known, we resort to a two-stage estimation procedure [9], where the estimated density obtained by performing standard KDE with a Gaussian kernel,  $\hat{\rho}_0(x)$  is used as a pilot estimate and this pilot estimate is used to obtain  $a(x)$  and  $p(x)$ . Furthermore, as shown in [31], by choosing  $a(x) = \hat{\rho}_0(x)$  and  $p(x) = (\hat{\rho}_0(x))^\gamma$ , where  $\gamma \in [0, 1]$ , we get an estimated density that is equivalent to performing KDE based on Gaussian kernels with variable mean and bandwidth. It has been shown in [9], that a choice of  $\gamma = 0.5$  gives rise to a model that employs both drift and diffusivity, resulting in an improvement of the estimated density when compared to the pilot estimate obtained through KDE.

The only missing piece in this discussion on density estimation procedure is the optimal choice of kernel bandwidth or mixing time. As mentioned in the beginning of this section, this parameter is usually chosen to minimize some loss function. In this paper, we use the Maximum Likelihood Cross-Validation (MLCV) score and choose the value of the parameter that maximizes this score. The MLCV score evaluates the average, over each data point, of the log-likelihood of the estimated density obtained using all the other data-points,

$$MLCV(t) = \frac{1}{M} \sum_{i=1}^M \log \hat{\rho}_{-i}(x_i, t), \quad (25)$$

where  $\hat{\rho}_{-i}(x, t)$  is the density estimated using the same value of  $t$ , but with all the data points except  $x_i$ .  $\hat{\rho}_{-i}(x, t)$ , known as the

leave-one estimator, is obtained by modifying the initial condition to the diffusion equation (Eq. (24)) to

$$\hat{\rho}(x, 0) = \frac{1}{M-1} \sum_{j=1, j \neq i}^M \delta(x - x_j). \quad (26)$$

The value of  $t$  that maximizes this score is chosen as the optimal mixing time,  $t^*$ , over which Eq. (23) is solved for all the data points.

### 3.1.2. Density estimation of MEMS parameters

Having developed the theory of generating a stochastic model based on the given data, we apply it to model the uncertainties in some of the input parameters of the MEM devices described in Section 2. Specifically, we look at uncertainties in the elastic modulus and thermal conductivity of the movable electrode as well as in the inter-electrode gap between the two electrodes. The reason for selecting these parameters is that variations in these quantities would directly lead to uncertainties in the mechanical, thermal and electrical fields, respectively. Moreover, due to the coupled nature of the physical model, it would be interesting to see how they propagate through the system and affect the device displacement, which is our ultimate output parameter of interest. Although there may be many more sources of uncertainty in an actual device, we restrict our focus in this paper to the above three variable parameters only. The experimental data that is used to model the uncertainties in these parameters has been obtained from previous material characterization studies available in the literature.

In this paper, we assume that the micromechanical devices under consideration are fabricated using surface micromachining technology. We assume that the material that comprises the movable electrode is isotropic and uniform. The ground plate is fabricated using the same process, but has a thin film coating of a material of high electrical conductivity to ensure that it behaves like a metal. Since one of our uncertain parameters is thermal conductivity, we ignore temperature-dependent nonlinearities that would normally be considered in a realistic physical model, because of the additional complexity that temperature-dependence introduces in the stochastic model. The dielectric medium surrounding the electrodes is assumed to be air.

In order to characterize the uncertainty in the elastic modulus, we look at changes in Young's modulus of polysilicon due to variations in the fabrication process. Devices that use polysilicon are most commonly fabricated using low pressure chemical vapor deposition (LPCVD). The nature of the deposition process is such that the final polysilicon films have widely varying material properties depending on conditions under which they were fabricated. A study performed by Lee et al. [32] looks at the effect of deposition temperature and phosphorous doping on the Young's modulus of polysilicon films. A stochastic model based on this experimental data is given in [9], where a generalized diffusion-based model has been used to estimate the probability density function that corresponds to the randomness in the data. The data and the resulting PDF are shown in Fig. 3.

We perform a similar procedure to create a stochastic model for thermal conductivity. We use heterogeneous measurements of thermal conductivity of silicon from the literature and construct a stochastic model using that data. Since these measurements are obtained from experiments conducted by independent research groups, they represent the thermal conductivity of the same material fabricated under different conditions and tested using different experimental setups. Fig. 4 shows the thermal conductivity data and the estimated PDF.

Finally, we look at the uncertainty in the air gap between the two electrodes. Depending on the micromachining processes used to fabricate the device, there may be a wide range of sources of uncertainty that may contribute to the variation in dimensional

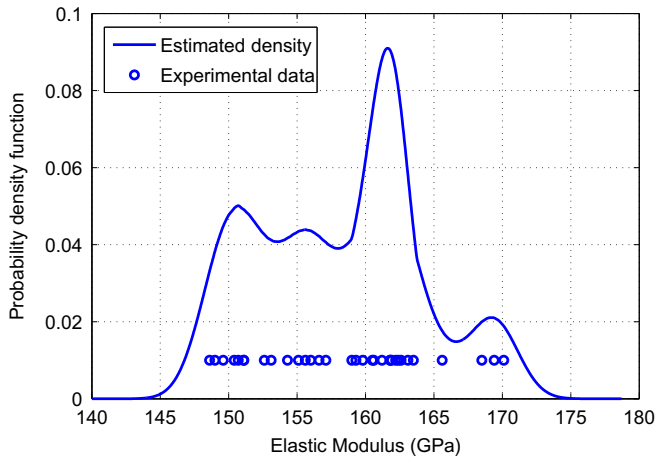


Fig. 3. PDF describing uncertainty in Young's modulus of polysilicon due to LPCVD process variations. The density was generated using the generalized diffusion-based estimator with  $\gamma = 0.5$ . The circles represent the experimental data.

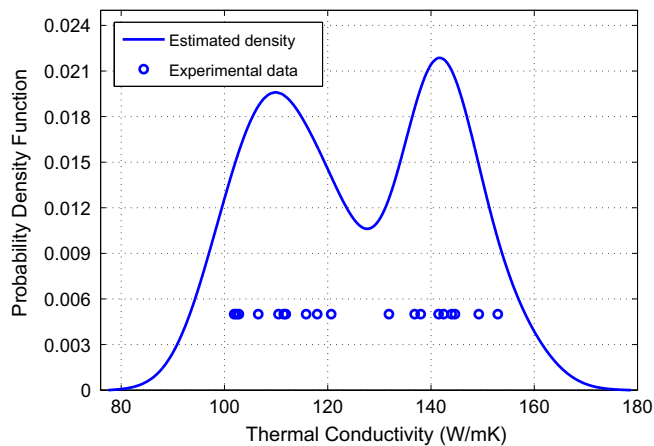


Fig. 4. PDF describing uncertainty in thermal conductivity of silicon from heterogeneous measurements. The density was generated using the generalized diffusion-based estimator with  $\gamma = 0.5$ .

parameters, e.g. misalignment in photolithography, variations in the etching rate, etc. Since the randomness in geometric parameters is highly specific to the device and the manufacturing process, it is not possible to develop a generic stochastic model for the air gap using results from similar studies in the literature, as is shown above for the other two parameters. As a result, except in the case where dimensional data is available for a specific device, the best option is to assume that the inter-electrode gap varies according to some standard distribution. In this paper, we assume that the gap varies uniformly on either side of the nominal value. The range of variation is specified for each MEMS example that we consider.

### 3.2. Propagation of uncertainties

Using the stochastic models generated above, we can propagate the uncertainties in the inputs through the micromechanical system and examine the statistics of the output quantities that we are interested in. Conceptually, this is achieved by replacing the system of equations described in Section 2 by their stochastic equivalents, where some of the terms are no longer deterministic, but rather have uncertainties associated with them. We make the assumption that the number of sources of uncertainty that are

present in the equations is finite and that these sources are all independent. This means that the input stochastic model can be characterized by a finite set of independent random variables, whose joint probability distribution can be decomposed into a product of marginal distributions of individual variables. Denoting the number of such random variables as  $n$ , we seek the solution to the system of equations describing the device, in the  $n$ -dimensional random space,  $\mathcal{H}^n$ , spanned by these variables. Furthermore, we assume that the range of values that each of the random variables can take is continuous and bounded, i.e. the sample space of each random variable is a bounded interval in  $\mathbb{R}$ . Together with the assumption that the variables are independent, this implies that  $\mathcal{H}^n$  can be represented as an  $n$ -dimensional hypercube in the random space.

The propagation of uncertainties has been the topic of a lot of research and a variety of methods have been developed that perform this task efficiently. Traditionally, the most popular among these are sampling-based methods, like the Monte Carlo method, which randomly draw independent samples from the input space. Each sample is a point,  $\xi \in \mathcal{H}^n$ , which represents one random realization of the uncertain variables. The stochastic system is evaluated at each sample point to obtain the corresponding response and these responses are aggregated to obtain statistics of the desired output quantity. Although, sampling-based methods offer the advantage of being able to propagate stochastic models without intrusive modification of the numerical simulation code, they necessitate the evaluation of the system at a large number of samples in order to obtain statistics with a reasonable degree of accuracy. In the case of many MEMS examples, obtaining a deterministic solution for one realization of the uncertain parameters may itself be time-consuming, because it may involve numerically solving a complicated multiphysics model. Despite the development of more efficient methods like quasi-Monte Carlo methods [33], sampling-based methods converge slowly to the stochastic solution and are computationally expensive for estimating uncertainty in MEMS devices.

#### 3.2.1. Stochastic collocation

In this paper, we use the stochastic collocation (SC) method [17,34] for uncertainty propagation. Stochastic collocation interpolates the output solution as a sum of nodal values weighted by basis functions. Instead of evaluating the system at randomly sampled points, the stochastic differential equations are collocated at a pre-determined set of nodal points in the random space. By selecting the location of the nodes and the corresponding basis functions efficiently, a sparse multivariate interpolation scheme is obtained, which can be used to perform the collocation. The sparse interpolant takes advantage of the regularity in the stochastic solution to obtain a good approximation of the output solution using a much smaller number of system evaluations [35]. Given a function,  $f(\xi)$ , that describes the dependence of the stochastic solution on the uncertain parameters, we can approximate it using the interpolant,  $\mathcal{I}f$ , given by,

$$\mathcal{I}f(\xi) = \sum_{i=1}^N f(\xi_i) L_i(\xi), \quad (27)$$

where  $\xi_i$  and  $L_i(\xi)$  denote the  $i$ th node in the random domain and its corresponding basis function, respectively. The basis functions satisfy the property that  $L_i(\xi_j) = \delta_{ij}$ ,  $\forall 1 \leq i, j \leq N$ . When using the SC method for micromechanical devices, almost all the computational effort is spent in evaluating the stochastic solution at each node,  $f(\xi_i)$ , and hence, this scales with the number of nodes,  $N$ , in the multivariate grid. Therefore, it is imperative to choose an interpolation scheme that economizes on the number of nodal evaluations.

We follow the procedure for construction of an efficient multivariate interpolation scheme as described in [20], by first constructing a family of univariate grids for each dimension in the random space. Consider, for example, any one dimension in this space that corresponds to one of the random variables. We construct sequences of univariate gridpoints,  $\chi^k$ , where each sequence contains  $m^k$  gridpoints, i.e.,  $\chi^k = \{\xi_j^k, j = 1, 2, \dots, m^k\}$ . The grid points lie within the range of values that this random dimension can take and can be expressed as  $\xi_j^k = a + (b - a)\eta_j^k$ , where  $a$  and  $b$  are the minimum and maximum values, respectively, that this random variable takes, while  $\eta_j^k \in [0, 1]$  is the normalized co-ordinate corresponding to each gridpoint. We choose the normalized co-ordinates according to the rule,

$$m^k = \begin{cases} 1 & \text{if } k = 1, \\ 2 & \text{if } k = 2, \\ 2^{k-2} & \text{if } k > 2, \end{cases} \quad (28)$$

$$\eta_j^k = \begin{cases} 0.5 & \text{for } j = 1 \text{ if } k = 1, \\ 0, 1 & \text{for } j = 1, 2 \text{ if } k = 2, \\ \frac{2j-1}{2m^k} & \text{for } j = 1, 2, \dots, m^k \text{ if } k > 2. \end{cases} \quad (29)$$

For each of these gridpoints, we choose corresponding piecewise linear basis functions,  $l_j^k(\xi(\eta))$ , which are given by,

$$l_j^k(\xi(\eta)) = \begin{cases} 1 & \text{for } j = 1 \text{ when } k = 1, \\ \max(0, 1 - 2|\eta - \eta_j^k|) & \text{for } j = 1, 2 \text{ when } k = 2, \\ \max(0, 1 - 2m^k|\eta - \eta_j^k|) & \text{for } j = 1, 2, \dots, m^k \text{ when } k > 2, \end{cases} \quad (30)$$

where  $\eta \in [0, 1]$  is any arbitrary point in the normalized range for the random variable under consideration, while  $\xi(\eta)$  is the corresponding value in the sample space of the random variable. Fig. 5(a) shows the univariate grids and their corresponding basis functions for  $k = 1, 2, 3$ . If we fix the maximum level of interpolation to be  $k$  along each dimension, we can construct sequences of univariate grids and basis functions along each random dimension as shown above. Using these, it is possible to conceive of a naive multivariate interpolation scheme where we simply take tensor products of all possible combinations of grids along each dimension. However, it can be shown that this would yield a scheme that requires  $N = (\sum_{i=1}^k m^i)^n$  nodal evaluations, which becomes very expensive as  $n$  increases.

A better way of generating a sparser multivariate grid is to use the Smolyak algorithm [36]. Instead of using tensor products of all univariate grid combinations, the Smolyak algorithm retains only selected tensor products that are chosen according to a special

rule. Consequently, it achieves the goal of reducing the number of nodes in the interpolation scheme, while maintaining the quality of interpolation up to a logarithmic factor [35]. We consider the interpolation of a function,  $f$ , defined on  $\mathcal{H}^n$  and define a parameter,  $q = 0, 1, 2, \dots$ , which denotes multivariate interpolation level. We construct a sparse interpolant,  $A_{q,n}(f)$ , in a hierarchical fashion with  $A_{-1,n}(f) = 0$  as,

$$A_{q,n}(f) = A_{q-1,n}(f) + \Delta A_{q,n}(f), \quad (31)$$

where  $\Delta A_{q,n}(f)$  is the incremental interpolant corresponding to an interpolation level of  $q$ , given by,

$$\Delta A_{q,n}(f) = \sum_{|\mathbf{k}|=n+q} \sum_{\mathbf{j}} l_{\mathbf{j}}^{\mathbf{k}} \cdot \underbrace{(f(\xi_{\mathbf{j}}^{\mathbf{k}}) - A_{q-1,n}(f)(\xi_{\mathbf{j}}^{\mathbf{k}}))}_{\omega_{\mathbf{j}}^{\mathbf{k}}}, \quad (32)$$

where  $\mathbf{k}$  is the vector of length  $n$ , whose components  $k_j$  are the interpolation levels along each random dimension and  $|\mathbf{k}| = k_1 + \dots + k_n$  is the sum of these levels. For each  $\mathbf{k}$  such that  $|\mathbf{k}| = n + q$ , we perform a tensor product of univariate grids along each dimension that correspond to the components of  $\mathbf{k}$  and evaluate the function at those points. For each  $\mathbf{k}$ , there are  $M^{\mathbf{k}} = m^{k_1} m^{k_2} \dots m^{k_n}$  gridpoints that are added to the interpolant. The multi-index,  $\mathbf{j} = (j_1, j_2, \dots, j_n)$ , where each individual index,  $j_i$ , takes the values  $1, \dots, m^{k_i}$ , is used to index these gridpoints.  $l_{\mathbf{j}}^{\mathbf{k}} = l_{j_1}^{k_1} \otimes \dots \otimes l_{j_n}^{k_n}$  is the multivariate basis function corresponding to each gridpoint,  $\xi_{\mathbf{j}}^{\mathbf{k}}$ . We observe that in the incremental interpolant, the basis functions are weighted by the coefficients,  $\omega_{\mathbf{j}}^{\mathbf{k}}$ , which are defined as the *hierarchical surpluses* corresponding to each gridpoint. The hierarchical surpluses are computed by taking the difference between the function value and the interpolated value from the lower order interpolant evaluated at each new gridpoint. In other words, the interpolation is performed hierarchically, where new gridpoints are added at each new level and the difference between the actual function value and the previous interpolant is stored as the coefficient that weights the basis function at each new gridpoint. Fig. 5(b) gives an example of a sparse grid generated on a two-dimensional space using the Smolyak algorithm with  $q = 2$ . We see that the sparse grid uses only 13 nodes as opposed to a full tensor product grid, which would have used 25 nodes.

### 3.2.2. Adaptive stochastic collocation

The standard Smolyak algorithm uses the parameter,  $q$ , to determine the level of interpolation. As  $q$  is increased, the grid is refined over the entire domain by adding new gridpoints corresponding to the new value of  $q$ . However, in some situations, uniform refinement of the grid over the entire random space may be unnecessary and even, wasteful. This is especially true in cases where the stochastic solution is discontinuous in the random input

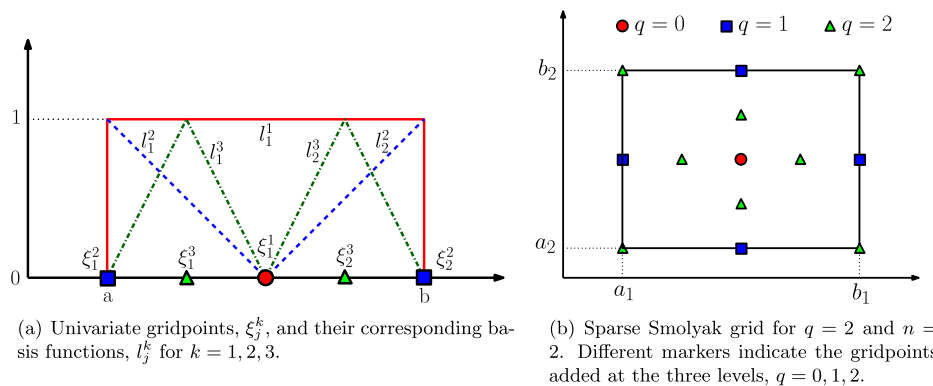


Fig. 5. Sparse multivariate grid generation process, starting from (a) the univariate grid, to create (b) the multivariate grid, using Smolyak algorithm. We see that the Smolyak algorithm uses only 13 points, whereas a full tensor product of two univariate grids would have generated a grid with 25 points.

space, e.g., in electrostatic microactuators, variations in the gap between the electrodes can cause the system to go from a stable solution to the onset of the pull-in instability, for specific values of the potential difference. In such situations, a local refinement strategy [19] is preferred so that extra gridpoints are added in regions where the error in the solution is large.

One such adaptive refinement strategy is explored in [20], wherein the original random domain is successively decomposed into subdomains in an effort to localize and reduce large errors. Each subdomain is interpolated using a coarse interpolant (i.e. by using a low value of  $q$ , denoted as  $q_0$ ), which is then used to estimate the interpolation error in that subdomain. Subdomains that do not satisfy appropriate error tolerance criteria are repeatedly sub-divided until the error is reduced to within acceptable limits. It is shown that for discontinuous functions, this process is more efficient in reducing the interpolation error than the standard Smolyak refinement method using a comparable number of gridpoints.

The key idea behind the adaptive refinement strategy is that for a given value of  $q$ , the incremental interpolant defined in Eq. (32) adjusts the result from the previous interpolation level by including new gridpoints and by adding corrections (hierarchical surpluses) to the interpolant at these points. The absolute value of these hierarchical surpluses decreases as the function gets interpolated better. This motivates the use of the hierarchical surpluses corresponding to the gridpoints at the highest level of the sparse interpolant, as error indicators for adaptive analysis. We assume that the original domain,  $\Gamma$ , is decomposed into  $N_d$  non-overlapping subdomains, each of which is interpolated using the coarse interpolant with an interpolation level of  $q_0$ . We define the interpolation error in the  $s$ -th subdomain,  $\Gamma_s$ , as,

$$\beta_s = \max_{|k|=n+q_0} |\omega_j^k|, \quad (33)$$

where we choose the interpolation error,  $\beta_s$  to be the maximum absolute value among the hierarchical surpluses at the highest level. Using this error, we formulate the first error tolerance criterion, in which we consider a subdomain for splitting if its interpolation error satisfies the condition,

$$\beta_s J_s \geq \tau_1, \quad (34)$$

where  $J_s$  is the volume of the subdomain and  $\tau_1$  is a tolerance parameter that is prescribed in advance. In addition to this condition, we also use a second criterion to identify the important dimensions along which the subdomain is to be split. For each dimension,  $i = 1, \dots, n$ , we define a second error indicator,  $\gamma_i$ , as,

$$\gamma_i = \sum_{\mathbf{k}_i, \mathbf{j}} (\omega_j^{\mathbf{k}_i})^2, \quad \mathbf{k}_i = \{\mathbf{k} : k_i = q_0 + 1, k_j = 1 \forall j \neq i\}, \quad (35)$$

For each dimension,  $i$ ,  $\gamma_i$  picks the gridpoints that come from the tensor product of the univariate grid of level  $q_0 + 1$  along dimension  $i$ , with the lowest univariate grid of level 1 along all the other dimensions. The hierarchical surpluses corresponding to these gridpoints provide an estimate of the interpolation error along the dimension  $i$ , which is stored in the error indicator,  $\gamma_i$ . Using the value of  $\gamma_i$  along each dimension, we define the second error tolerance criterion to identify the sensitive random dimensions as the ones which satisfy,

$$\gamma_i \geq \tau_2 \max_{j=1, \dots, n} \gamma_j, \quad 0 < \tau_2 < 1, \quad (36)$$

where  $\tau_2$  is a tolerance parameter that is usually chosen to be 0.5. Once the sensitive dimensions are identified, the subdomain is split into two equal halves along each of those dimensions. The algorithm starts off by interpolating the original domain. During each iteration, all the subdomains that need refinement (according to Eq. (34)) are identified and split along their sensitive dimensions (as per Eq. (36)). This is done until the global interpolation error

drops below the specified tolerance  $\tau_1$ . The complete details of the algorithm for performing the adaptive refinement of the domain to reduce interpolation error, are given in [20].

### 3.2.3. Mean-weighted adaptive refinement

As stated previously in Section 1, the goal of this work is to create a framework for uncertainty analysis that will aid the design of MEMS devices. From this standpoint, one is usually interested not only in the final stochastic solution itself, but also in the statistics that describe the uncertainty. These statistics, usually mean and variance, are useful descriptors of the uncertainty in the device and are useful for comparison with experimental results. Given this situation, it is natural to expect that the uncertainty propagation method that we choose must also be guided by the same goal and must strive to reduce the error in these statistics with minimal number of system evaluations. The adaptive refinement strategy described in Section 3.2.2 is based on interpolation-weighted adaptive refinement (IWAR), where the goal is to reduce the interpolation error. This has the secondary effect of reducing the error in the statistics of the solution, as shown in [20]. However, in this work, we are interested in optimizing the method to reduce the error in one of the statistics, say the mean value of the stochastic solution. Hence, we seek a mean-weighted adaptive refinement strategy (MWAR), which adaptively decomposes the domain to reduce the error in the mean.

We motivate the MWAR strategy by first deriving the expressions for computing the statistics of the stochastic solution on the set of subdomains obtained from adaptive analysis. Given the function,  $f$ , that represents the stochastic solution that we are interested in, we compute its mean as,

$$\mathbb{E}[f] = \int_{\Gamma} f(\xi) \rho(\xi) d\xi = \sum_{s=1}^{N_d} \int_{\Gamma_s} f(\xi) \rho(\xi) d\xi, \quad (37)$$

where  $\rho(\xi)$  is the joint PDF of the stochastic model that we have chosen in Section 3.1. As mentioned above, due to the assumption of independence among the random variables,  $\rho(\xi)$  can be expressed as a product of marginal PDFs,  $\rho_i(\xi_i)$ ,  $i = 1, \dots, n$ , corresponding to each dimension. In order to compute the above integral, we replace the function,  $f(\xi)$ , in Eq. (37) by the sparse interpolant  $A_{q,n}(f)$ . We then use the relation in Eq. (31) to rewrite Eq. (37) as,

$$\mathbb{E}[f] \approx \sum_{s=1}^{N_d} \left[ \int_{\Gamma_s} A_{q-1,n} \rho(\xi) d\xi + \int_{\Gamma_s} \Delta A_{q,n} \rho(\xi) d\xi \right]. \quad (38)$$

The second term in Eq. (38) can be thought of as the correction to the value of the mean in the subdomain,  $\Gamma_s$ , using the gridpoints added at the topmost level. Using Eq. (32), we can rewrite this term as,

$$\int_{\Gamma_s} \Delta A_{q,n} \rho(\xi) d\xi = \sum_{|k|=n+q} \sum_{\mathbf{j}} \omega_j^k \int_{\Gamma_s} I_{\mathbf{j}}^k(\xi) \rho(\xi) d\xi. \quad (39)$$

This motivates us to define an error indicator,  $e_j^k$ , that is suitable for mean-weighted adaptive refinement, as,

$$e_j^k = \omega_j^k \int_{\Gamma_s} I_{\mathbf{j}}^k(\xi) \rho(\xi) d\xi. \quad (40)$$

Using this error indicator, we can define our adaptivity criteria in a similar manner as in Section 3.2.2. We decide to split a particular subdomain,  $\Gamma_s$ , if its error indicators satisfy,

$$\max_{|k|=n+q_0} |e_j^k| \geq \tau_1, \quad (41)$$

where  $\tau_1$  is a tolerance parameter similar to that used in Eq. (34). Furthermore, we replace  $\omega_j^k$  with  $e_j^k$  in Eq. (35) and use Eq. (36) to decide which are the sensitive dimensions along which the subdomain is to be split.

In order to implement this refinement technique, we identify a starting domain and successively refine it into smaller subdomains according to MWAR. The standard approach towards performing adaptive refinement is to perform the refinement in successive iterations. In each iteration, all subdomains that do not satisfy the error tolerance criterion are chosen for splitting. The direction along which splitting occurs is determined by the secondary error tolerance criterion. In the case of stochastic collocation, the solution in any one subdomain is independent of that in any other. Hence, the refinement process can be modified by choosing the subdomain that has the maximum error in each step and performing refinement only in that element. This is a more efficient utilization of computational resources because the refinement is performed only where it is most needed. This sequential mean-weighted adaptive refinement (SMWAR) technique can be efficiently implemented by putting all the subdomains in a special data-structure called a *heap* or *priority queue*. In this data structure, the subdomains are arranged as nodes in a binary tree with the special property that the node with the maximum error is always placed as the root of the tree. Operations that perform successive addition or deletion of nodes maintain this property of the tree. As a result, the subdomain with the maximum error can be fetched in  $\log N_d$  operations, where  $N_d$  is the number of subdomains. We use this sequential version of the MWAR method to implement the adaptive refinement operation.

#### 4. Numerical results

In this section, we present the numerical results obtained by performing uncertainty quantification on the electrostatic and hybrid ETM microactuators presented in Section 2. As mentioned before, we consider the stochastic models that have been developed for geometric and material parameters and propagate them through the physical system to look at the variation in output parameters of interest. Since we are primarily interested in obtaining the statistics of the outputs, we shall limit our focus to determining the mean and variance (or equivalently, standard deviation) of these quantities to a reasonable degree of accuracy. In this context, we shall show how the SMWAR method provides significant reduction in the computational time needed to compute these quantities. Since we perform numerical simulations of micromechanical devices, we measure computational time in terms of the number of function evaluations, where each evaluation is an instance of the numerical solver being run on a single

set of input parameters that corresponds to a point in the uncertain input space.

##### 4.1. Simulation of an electrostatic microactuator

We first consider the simple case of the electrostatic microswitch described in Section 2.2. The device under consideration consists of a polysilicon beam that is  $100\ \mu\text{m}$  long,  $1\ \mu\text{m}$  thick and  $10\ \mu\text{m}$  wide in the direction perpendicular to the cross-sectional plane shown in Fig. 2. The beam is clamped at its left end, while the right end is free to move. It is separated from the ground plate by the inter-electrode gap, which varies uniformly in the range  $[1.8, 2.2]\ \mu\text{m}$ . This corresponds to a 10% variation on either side of the mean value of  $2\ \mu\text{m}$ . A potential difference,  $V$ , is applied between the two electrodes, causing the movable beam to deflect towards the ground plate under the action of electrostatic force. The potential difference is varied between 6 and 10 V. We measure the displacement of the tip of the beam from its original position. In addition to the uncertainty in the gap, the Young's modulus of the beam is assumed to vary between 140 GPa and 178.7 GPa, according to the stochastic model described in Section 3.1.2. Together, these two models describe the variation in input parameters of a typical electrostatic microactuator due to uncertainties that are encountered in microfabrication processes. The goal is to compute the mean and variance of the actuator displacement as a result of randomness in the gap and elastic modulus. We use a tolerance value of  $\tau_1 = 10^{-5}$  to specify the desired level of accuracy in the value of the mean displacement that is computed. Each subdomain uses a coarse interpolant with the level  $q_0 = 2$ , which corresponds to a grid of 13 points per subdomain in the two-dimensional random input space.

The stochastic tip displacement is plotted as a function of the uncertain parameters in Fig. 6(a) for a potential difference of 10 V. Fig. 6(b) shows the PDF of this stochastic solution. We use both IWAR and SMWAR to propagate the uncertainties in Young's modulus and inter-electrode gap through the device model. The final set of gridpoints generated by these adaptive refinement methods for the case  $V=10$ , is shown in Fig. 7. These gridpoints correspond to the sets of parameter values for which the tip displacement is computed in order to construct the interpolant that approximates the stochastic solution. We see that the SMWAR method uses fewer function calls to construct an interpolant. We compare the accuracy of the interpolation in terms of the error in the statistics of the stochastic tip displacement. Table 1 shows the results of the uncertainty quantification for different values

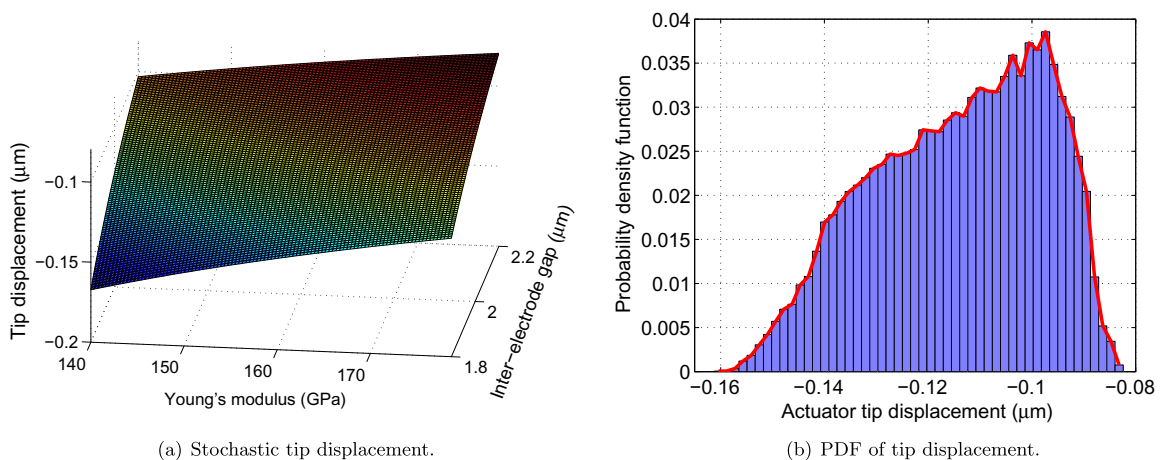


**Fig. 6.** Stochastic tip displacement computed from the UQ of an electrostatic microactuator for a potential difference of 10 V. (a) Tip displacement (shown on the z-axis) as a function of the variation in Young's modulus (shown on the x-axis in GPa) and inter-electrode gap (shown on the y-axis in  $\mu\text{m}$ ). (b) PDF of the output tip displacement.

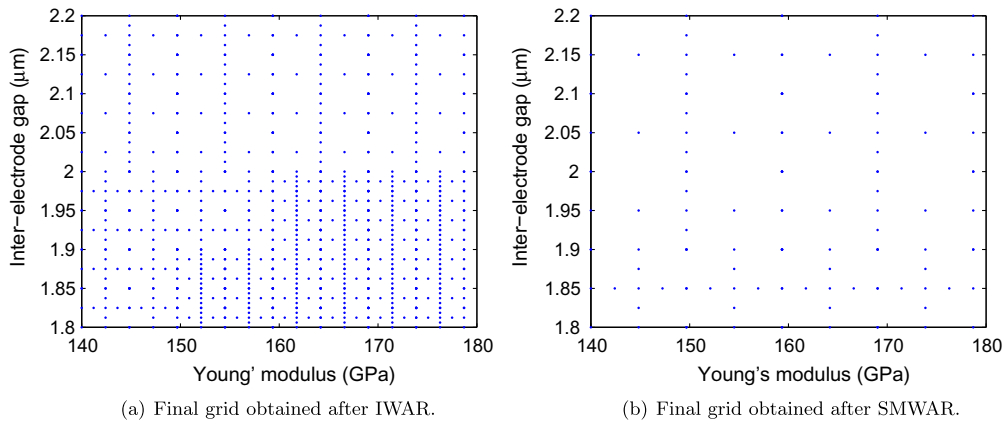


**Fig. 7.** Final grids obtained after adaptive refinement of the stochastic solution of the electrostatic microactuator for a potential difference of 10 V. We see that the grid generated by the IWAR method, shown in (a), uses 884 nodes while the SMWAR grid, shown in (b), uses only 130 nodes to compute the stochastic solution.

**Table 1**  
Variation of electrostatic microactuator tip displacement due to uncertain gap, and Young's modulus.

Potential difference (V)	Mean			Variance		
	SMWAR	IWAR	Difference	SMWAR	IWAR	Difference
6	-0.037873	-0.037839	$3.5 \times 10^{-5}$	0.000054	0.000054	0
7	-0.052163	-0.052122	$4.1 \times 10^{-5}$	0.000103	0.000104	$1 \times 10^{-6}$
8	-0.069113	-0.069061	$5.1 \times 10^{-5}$	0.000185	0.000186	$1 \times 10^{-6}$
9	-0.088977	-0.088917	$6.0 \times 10^{-5}$	0.000315	0.000316	$1 \times 10^{-6}$
10	-0.112069	-0.112013	$5.5 \times 10^{-5}$	0.000518	0.000519	$1 \times 10^{-6}$

of the potential difference used to actuate the device. We see that in each case, the SMWAR method yields statistics that are comparable to those obtained using IWAR, showing that the differences between the mean values obtained in either case are of the order of  $\tau_1$ . Finally, we compare the number of function calls made by each method while computing the statistics of the solution. We know that for the given range of voltages applied, the actuator tip varies nonlinearly with varying gap and Young's modulus, but the voltage is small enough to avoid the pull-in instability. Hence, we expect that both the refinement methods should be able to accurately compute the output statistics with relatively few function calls. Table 2 compares the number of function calls made by either algorithm for each value of the potential difference. In each case, we see that the number of function evaluations made by the SMWAR method is about 6–8 times lower than the corresponding number for IWAR. This demonstrates that SMWAR uses a much smaller number of function calls to obtain a value of mean with an accuracy of the order of the tolerance used.

#### 4.2. Simulation of a hybrid ETM microactuator

The hybrid ETM microactuator is a device that integrates electrostatic and electrothermal actuation. A detailed analysis of a typical hybrid ETM microactuator is given in [21]. We choose a device with the same dimensions and material parameters as that mentioned in that paper and perform uncertainty analysis on it, assuming that the Young's modulus and thermal conductivity of the movable electrode are uncertain and vary according to the stochastic models mentioned in Section 3.1.2. Furthermore, we assume that the gap between the electrodes varies uniformly in the range [2.8, 3.2]  $\mu\text{m}$ . Since the thermal conductivity is assumed to be uncertain, this uncertainty will propagate into the temperature field as well. For simplicity, we neglect all nonlinear variations of material parameters with temperature. We constrain the potential of terminals,  $V_2$  and  $V_g$ , to zero and apply a potential difference,  $V$ ,

**Table 2**  
Number of function calls used in the UQ of the electrostatic microactuator.

Potential difference $\rightarrow$	$V = 6$	$V = 7$	$V = 8$	$V = 9$	$V = 10$
SMWAR	65	91	104	104	130
IWAR	546	546	572	676	884

on  $V_1$  with respect to the other two. The value of this potential difference is varied from 6 to 10 V and in each case, we examine the uncertainty of the displacement of the actuator tip due to the variation in input parameters. As in the previous case, we limit the potential difference to a range such that the stochastic solution is continuous for the given range of uncertainty. We use a value of  $\tau_1 = 10^{-5}$  in the tolerance criterion to determine when to stop domain decomposition. Each subdomain uses a coarse interpolant with the level  $q_0 = 2$ , which corresponds to a grid of 25 points per subdomain in the three-dimensional random input space.

The variation of the stochastic tip displacement with the three uncertain parameters is shown in Fig. 8(a) for a potential difference of 10 V along specific slices in random domain. Fig. 8(b) shows the PDF of this stochastic solution. Table 3 shows the mean and variance of the actuator tip displacement as obtained using the SMWAR and IWAR methods. We see that both methods produce results that are very close to each other, with the difference being of the order of  $\tau_1$ . Table 4 shows the number of function calls used by either refinement technique. We see that the number of function calls made by the SMWAR method is up to 8 times lower than IWAR, especially for larger voltages, when the stochastic solution to be interpolated becomes more nonlinear.

#### 4.3. UQ in the presence of discontinuities

As described in [21], due to the integration of electrostatic force in addition to electrothermal expansion in the hybrid ETM actuator, it exhibits the *pull-in* instability for sufficiently large values

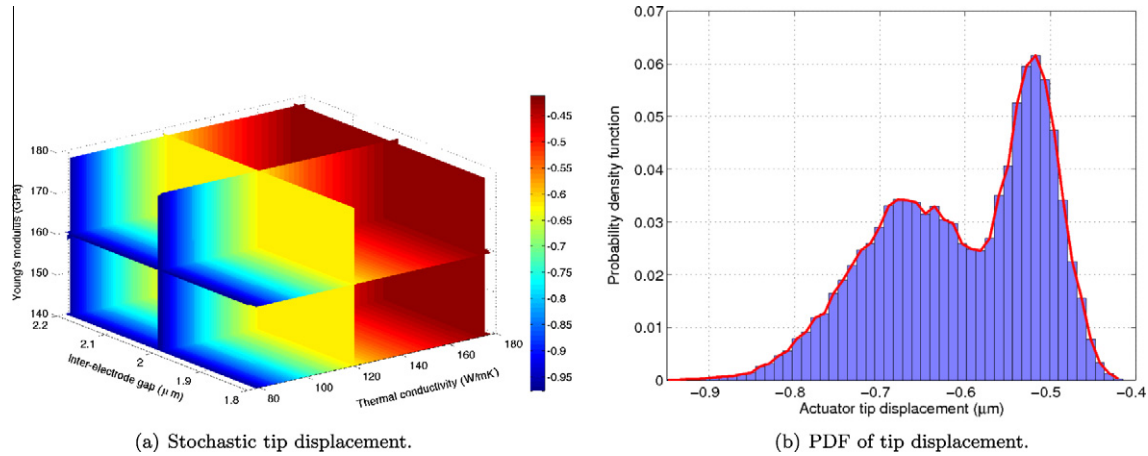


**Fig. 8.** Stochastic tip displacement of the hybrid ETM microactuator for a potential difference of 10 V. (a) Variation of tip displacement (indicated by color) with thermal conductivity (shown on the x-axis in W/mK), inter-electrode gap (shown on the y-axis in  $\mu\text{m}$ ) and Young's modulus (shown on the z-axis in GPa). The color bar on the right shows the corresponding value of the displacement. (b) PDF of the output tip displacement.

**Table 3**  
Variation of hybrid ETM actuator tip displacement due to uncertain gap, thermal conductivity and Young's modulus.

Potential difference (V)	Mean			Variance		
	SMWAR	IWAR	Difference	SMWAR	IWAR	Difference
6	-0.210398	-0.210380	$1.8 \times 10^{-5}$	0.002583	0.002580	$3 \times 10^{-6}$
7	-0.286433	-0.286415	$1.8 \times 10^{-5}$	0.004786	0.004781	$5 \times 10^{-6}$
8	-0.374212	-0.374201	$1.1 \times 10^{-5}$	0.008168	0.008163	$5 \times 10^{-6}$
9	-0.473791	-0.473775	$1.6 \times 10^{-5}$	0.013096	0.013086	$1.0 \times 10^{-5}$
10	-0.585219	-0.585198	$2.1 \times 10^{-5}$	0.019988	0.019973	$1.5 \times 10^{-5}$

**Table 4**  
Number of function calls used in the UQ of the hybrid ETM actuator.

Potential difference $\rightarrow$	V = 6	V = 7	V = 8	V = 9	V = 10
SMWAR	225	250	325	325	325
IWAR	800	800	800	2150	2250

of the potential difference applied to the device. The reason for this instability is the nonlinear increase in the electrostatic force compared to the mechanical restoring force, due to which a stable solution ceases to exist when the actuator displacement exceeds a certain critical value. As a result, the actuator tip crashes onto the ground plate and the device is deemed to have “pulled-in”. For a given set of material and device parameters, the smallest voltage at which this phenomenon occurs is called the *pull-in voltage*. The pull-in voltage depends on the initial gap between the electrodes, as well on as the stiffness and thermal conductivity of the movable electrode.

Since we are concerned with the stochastic displacement of the actuator tip, we note that when a stable solution exists, the displacement is some value between zero and the critical gap (approximately one-third of the inter-electrode gap for many electrostatic actuators). However, after pull-in occurs, the value of the displacement is equal to the gap, since the actuator tip has crashed onto the ground plate. In the presence of uncertainties in input parameters, it is possible that for the same value of potential difference, the actuator displacement has a stable solution in some parts of the domain, while it exhibits pull-in elsewhere. This creates a sharp discontinuity in the stochastic solution that is to be interpolated. As mentioned in Section 3.2.2, adaptive refinement techniques work well to localize the error due to the discontinuity and are able to interpolate the stochastic solution with fewer points.

In this section, we compare the performance of the two adaptive refinement techniques in estimating the statistics of the

solution. We consider the same hybrid ETM device as in the previous section. We assume that the source of uncertainty is restricted to thermal conductivity and inter-electrode gap. The stochastic model for thermal conductivity is assumed to be the same as that described in Section 3.1.2, while the gap is assumed to vary uniformly in the range  $[1.8, 2.2] \mu\text{m}$ , which corresponds to a 10% variation on either side of the mean value of  $2 \mu\text{m}$ . We use a value of  $\tau_1 = 10^{-5}$  and  $q_0 = 2$  and vary the potential difference between 6 and 12 V.

Fig. 9 shows the tip displacement as a function of thermal conductivity and inter-electrode gap, when the potential difference is 10 V and 12 V. We see that for the latter case, the solution exhibits pull-in in a particular range of the uncertain parameters. As expected, we see that pull-in tends to occur when both the inter-electrode gap and the thermal conductivity are low. Table 5 shows the mean value and variance of the tip displacement for each value of potential difference. Again we see that the results obtained from SMWAR and IWAR methods are very close, with the difference being of the order of  $\tau_1$ . The deviation between the methods increases slightly for the case when potential difference is 12 V. This is expected, since the presence of a discontinuity causes small errors in the interpolated value of the solution, especially in the region near the discontinuity. Table 6 compares the performance of the two methods. Once again, the SMWAR technique produces comparable results with a much small number of function evaluations, showing the advantage of using a mean-weighted technique.

4.4. Experimental validation

In this section, we compare the results obtained using the UQ framework, with experimentally determined uncertainties in MEMS devices. We consider the micromechanical switch described in [37] shown in Fig. 10. The microswitch, fabricated using standard CMOS processes, consists of a square aluminium membrane

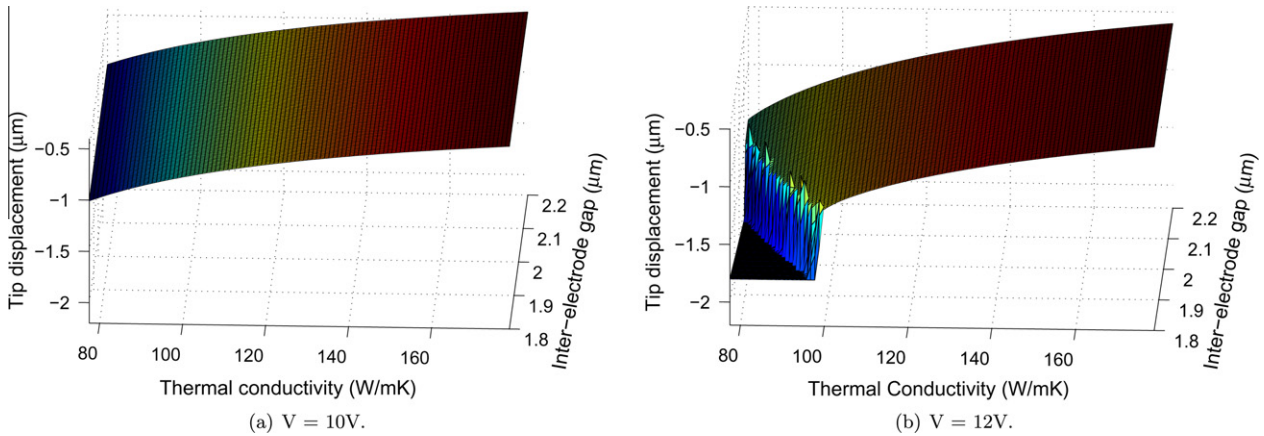


**Fig. 9.** Stochastic tip displacement (shown on the z-axis) as a function of the variation in thermal conductivity (shown on the x-axis in W/mK) and inter-electrode gap (shown on the y-axis in  $\mu\text{m}$ ). We see the onset of the pull-in instability for  $V = 12\text{ V}$ , which causes the value of tip displacement to be equal to the gap.

**Table 5**  
Variation of hybrid ETM actuator tip displacement due to uncertain gap and thermal conductivity.

Potential difference (V)	Mean ( $\mu\text{m}$ )			Variance ( $\mu\text{m}^2$ )		
	SMWAR	IWAR	Difference	SMWAR	IWAR	Difference
6	-0.218057	-0.218039	$1.8 \times 10^{-5}$	0.001181	0.001178	$3 \times 10^{-6}$
7	-0.297053	-0.297033	$1.9 \times 10^{-5}$	0.002194	0.002189	$5 \times 10^{-6}$
8	-0.388455	-0.388437	$1.8 \times 10^{-5}$	0.003757	0.003752	$5 \times 10^{-6}$
9	-0.492537	-0.492507	$3.0 \times 10^{-5}$	0.006069	0.006058	$1.0 \times 10^{-5}$
10	-0.609807	-0.609760	$4.7 \times 10^{-5}$	0.009398	0.009381	$1.6 \times 10^{-5}$
12	-0.896731	-0.896491	$2.40 \times 10^{-4}$	0.029064	0.028907	$1.57 \times 10^{-4}$

**Table 6**  
Number of function calls used in the UQ of the hybrid ETM actuator.

Potential difference $\rightarrow$	V = 6	V = 7	V = 8	V = 9	V = 10	V = 12
SMWAR	117	130	169	169	182	520
IWAR	520	572	975	1911	2366	3692

suspended by tethers at the corners, which is electrostatically actuated by a drive electrode. We examine the effect of variation in input parameters, like material properties of the membrane and the inter-electrode air gap, on the uncertainty in the actuator’s pull-in voltage. We use the same numerical model as the one described in [37] and show that the error bars reported with the experimental measurements in this paper are consistent with the uncertainties that we predict using our model. We use the variation in Young’s modulus of aluminium with process parameters [38], to generate a stochastic model for elastic modulus, and hence, the membrane stiffness (Fig. 11). Since the error in air gap values reported in [38] seem to be of the order of  $0.05\ \mu\text{m}$ , we assume a model where the air gap varies uniformly about the mean value by  $0.05\ \mu\text{m}$ .

To evaluate the performance of the UQ framework, we simulate each of the devices fabricated in [37] using the stochastic models described above. These devices differ in the length of the square membrane and the shape of the tethers used to suspend the membrane. In each case, we compute the uncertainty in the pull-in voltage of the switch. Fig. 12 shows the PDF of the pull-in voltage for the device employing straight tethers and a membrane of length  $100\ \mu\text{m}$ . We first compute the PDF assuming a uniform stochastic model (where the uncertain parameters vary uniformly) and compare this to the actual PDF obtained by propagating the data-driven stochastic model. We note that the nature of uncertainty changes drastically when the proper stochastic model is chosen, showing

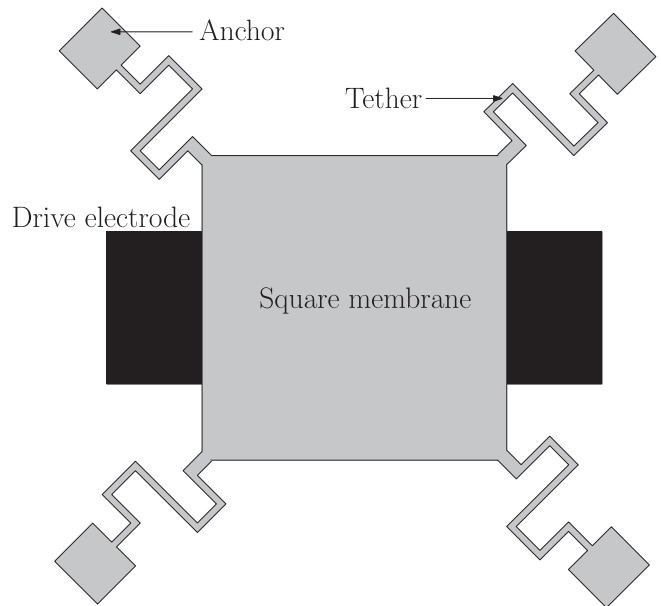


**Fig. 10.** Schematic of micromechanical switch that uses electrostatic actuation to drive a square membrane suspended by four tethers.

the importance of estimating the stochastic model using experimental data. We calculate the mean and standard deviation of the pull-in voltage for all the devices and compared them with corresponding results reported in [37] (see Table 7). We also compute the mean and standard deviation of the pull-in voltage under a uniform model. We see that the mean pull-in voltages predicted by our stochastic model compare very well with experimentally

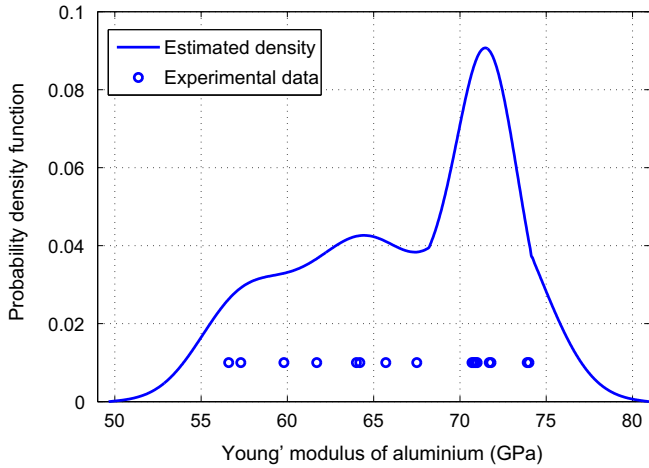


**Fig. 11.** Estimated PDF for Young's modulus of Al used in CMOS processes. Circles show the experimental data used for estimation.

determined values and lie within the error limits given in the experimental data. The calculated standard deviations are also of the same order of magnitude as the error in the data, showing that the uncertainty in the model has been captured reasonably well. The corresponding values for the uniform stochastic model show a good agreement in the value of the mean, but underestimate the standard deviation in the solution. The prediction accuracy

can be improved if more data is available to characterize the input uncertainty in the actual devices being tested. Thus we see that a proper analysis of the uncertainty in the device models helps to characterize the actual randomness in the device behaviour and aids in the design of micromechanical devices.

**5. Conclusions**

The goal of this study is to present a unified framework for performing uncertainty quantification in micromechanical systems. Restricting ourselves to electrothermomechanical actuators, we look at the hybrid ETM actuator, which integrates electrothermal and electrostatic actuation, as well as the standard electrostatic actuator, which is a special case of the hybrid ETM device. We identify three sources of uncertainty, Young's modulus, thermal conductivity and inter-electrode gap, which correspond to uncertainties in the mechanical, thermal and electric potential fields. Using data derived from experimental measurements, we construct stochastic models for each of these quantities by estimating their PDFs using density estimation. We also describe various techniques for the propagation of these stochastic models through the device. In particular, we focus on adaptive refinement methods based on decomposition of the input random domain. We motivate the use of the mean-weighted adaptive refinement method to efficiently compute the statistics of the stochastic solution.

The results that we obtain after performing UQ on the devices, show that the SMWAR method estimates the statistics of the

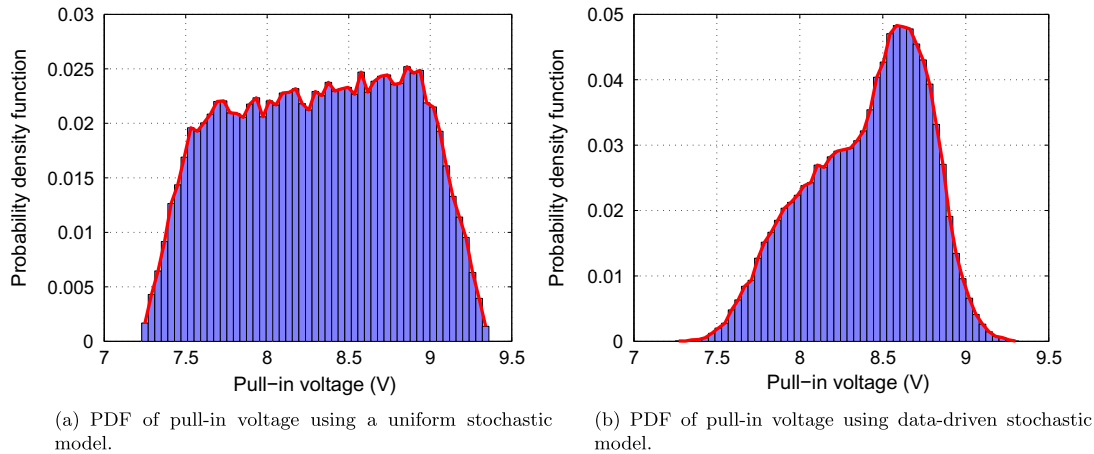


**Fig. 12.** PDFs of pull-in voltage obtained using different stochastic models, showing the drastic change in the distribution of output uncertainty with different input models.

**Table 7**  
Comparison of pull-in voltages in [37] with those obtained results using our stochastic model.

Device type <sup>a</sup>	Average air gap (μm)	Exp. pull-in voltage (V)	Est. pull-in voltage (V)	
			Uniform model	Data-driven model
Meander/200	1.75	4.2 ± 0.3	4.3 ± 0.2	4.2 ± 0.6
Meander/200	2.5	6.5 ± 0.5	6.6 ± 0.4	6.5 ± 1.0
Meander/200	2.65	7.5 ± 1.0	7.1 ± 0.4	7.0 ± 1.1
Meander/200	3.0	8.7 ± 1.5	8.3 ± 0.5	8.2 ± 1.4
Meander/100	1.75	8.7 ± 2.0	9.1 ± 0.6	8.9 ± 1.5
Meander/100	2.0	12.0 ± 2.0	10.9 ± 0.7	10.7 ± 1.8
Meander/100	2.1	11.5 ± 1.3	11.6 ± 0.8	11.5 ± 2.0
Meander/100	2.25	13.0 ± 1.3	12.8 ± 0.9	12.6 ± 2.2
Straight/200	0.85	3.8 ± 2.0	3.5 ± 0.2	3.9 ± 0.5
Straight/200	0.95	4.7 ± 1.0	4.0 ± 0.2	4.0 ± 0.6
Straight/200	1.1	5.2 ± 1.3	4.7 ± 0.3	4.7 ± 0.7
Straight/100	0.95	8.5 ± 1.5	7.7 ± 0.5	7.6 ± 1.3
Straight/100	1.05	9.5 ± 1.5	8.8 ± 0.6	8.7 ± 1.5

<sup>a</sup> Shape of the tethers and the length of the square membrane in μm.

stochastic solution quite accurately when compared to IWAR, with deviations of the order of the tolerance parameter used. However, the SMWAR method is able to produce these results with a much smaller number of function evaluations. We show improvement in performance that is almost of an order of magnitude in many cases. In the case of micromechanical devices, since each function evaluation corresponds to a run of the deterministic solver, this translates into a huge savings in computational time and effort.

### Acknowledgements

This work is supported by the National Science Foundation under Grant Nos. 0810294 and 0941497, and by the Department of Energy. The authors gratefully acknowledge the use of the Turing cluster maintained and operated by the Computational Science and Engineering Program at the University of Illinois. Turing is a 1536-processor Apple G5 X-serve cluster devoted to high performance computing in engineering and science.

### References

- [1] S.D. Senturia, N. Aluru, J. White, Simulating the behavior of MEMS devices: computational methods and needs, *IEEE Comput. Sci. Engrg.* 4 (1997) 30–43.
- [2] G. Li, N. Aluru, Efficient mixed-domain analysis of electrostatic MEMS, *IEEE Trans. Comput.-Aid. Des. Integr. Circ. Syst.* 22 (2003) 1228–1242.
- [3] S. De, N.R. Aluru, Full-Lagrangian schemes for dynamic analysis of electrostatic MEMS, *J. Microelectromech. Syst.* 13 (2004) 737–758.
- [4] S. Telukunta, S. Mukherjee, Fully Lagrangian modeling of MEMS with thin plates, *J. Microelectromech. Syst.* 15 (4) (2006) 795–810.
- [5] R. Ghosh, S. Mukherjee, Fully Lagrangian modeling of dynamics of MEMS with thin beams – Part I: Undamped vibrations, *J. Appl. Mech.* 76 (5) (2009) 051007.
- [6] R. Ghosh, S. Mukherjee, Fully Lagrangian modeling of dynamics of MEMS with thin beams – Part II: Damped vibrations, *J. Appl. Mech.* 76 (5) (2009) 051008.
- [7] C. Goldsmith, J. Ehmke, A. Malczewski, B. Pillans, S. Eshelman, Z. Yao, J. Brank, M. Eberly, Lifetime characterization of capacitive RF MEMS switches, in: *IEEE MTT-S International Microwave Symposium Digest*, vol. 1, 2001, IEEE Phoenix, AZ, USA, pp. 227–230.
- [8] D. Xiu, G. Karniadakis, Modeling uncertainty in flow simulations via generalized polynomial chaos, *J. Comput. Phys.* 187 (2003) 137–167.
- [9] N. Agarwal, N. Aluru, A data-driven stochastic collocation approach for uncertainty quantification in MEMS, *Int. J. Numer. Methods Engrg.* 83 (5) (2010) 575–597.
- [10] M. Liu, K. Maute, D.M. Frangopol, Multi-objective design optimization of electrostatically actuated microbeam resonators with and without parameter uncertainty, *Reliab. Engrg. Syst. Safety* 92 (10) (2007) 1333–1343.
- [11] J. Han, B. Kwak, Robust optimal design of a vibratory microgyroscope considering fabrication errors, *J. Micromech. Microeng.* 11 (6) (2001) 662.
- [12] J. Wittwer, M. Baker, L. Howell, Robust design and model validation of nonlinear compliant micromechanisms, *J. Microelectromech. Syst.* 15 (1) (2006) 33–41.
- [13] O. Le Maître, O. Knio, H. Najm, R. Ghanem, Uncertainty propagation using Wiener–Haar expansions, *J. Comput. Phys.* 197 (1) (2004) 28–57.
- [14] O. Le Maître, H. Najm, R. Ghanem, O. Knio, Multi-resolution analysis of Wiener-type uncertainty propagation schemes, *J. Comput. Phys.* 197 (2) (2004) 502–531.
- [15] D. Xiu, G. Karniadakis, The Wiener–Askey polynomial chaos for stochastic differential equations, *SIAM J. Sci. Comput.* 24 (2) (2002) 619–644.
- [16] X. Wan, G. Karniadakis, An adaptive multi-element generalized polynomial chaos method for stochastic differential equations, *J. Comput. Phys.* 209 (2) (2005) 617–642.
- [17] D. Xiu, J. Hesthaven, High-order collocation methods for differential equations with random inputs, *SIAM J. Sci. Comput.* 27 (2005) 1118–1139.
- [18] B. Ganapathysubramanian, N. Zabararas, Sparse grid collocation schemes for stochastic natural convection problems, *J. Comput. Phys.* 225 (1) (2007) 652–685.
- [19] X. Ma, N. Zabararas, An adaptive hierarchical sparse grid collocation algorithm for the solution of stochastic differential equations, *J. Comput. Phys.* 228 (8) (2009) 3084–3113.
- [20] N. Agarwal, N. Aluru, A domain adaptive stochastic collocation approach for analysis of MEMS under uncertainties, *J. Comput. Phys.* 228 (20) (2009) 7662–7688.
- [21] A. Alwan, N. Aluru, Analysis of hybrid electrothermomechanical microactuators with integrated electrothermal and electrostatic actuation, *J. Microelectromech. Syst.* 18 (5) (2009) 1126–1136.
- [22] D.S. Chandrasekharaiah, L. Debnath, *Continuum Mechanics*, Academic Press, 1994.
- [23] H. Parkus, *Thermoelasticity*, Blaisdel Publishing Company, New York, 1968.
- [24] P. Yarrington, D.E. Carlson, Successive approximations in nonlinear thermoelasticity, *Int. J. Engrg. Sci.* 14 (1976) 113–125.
- [25] H.A. Haus, J.R. Melcher, *Electromagnetic Fields and Energy*, Prentice Hall, 1989.
- [26] M. Jaswon, G. Symm, *Integral Equation Methods in Potential Theory and Elastostatics*, Academic Press, New York, 1977.
- [27] F. Shi, P. Ramesh, S. Mukherjee, On the application of 2D potential theory to electrostatic simulation, *Commun. Numer. Methods Engrg.* 11 (8) (1995) 691–701.
- [28] M.P. Wand, M.C. Jones, *Kernel Smoothing*, Chapman & Hall, London, 1995.
- [29] P. Chaudhuri, J. Marron, Scale space view of curve estimation, *Ann. Statist.* 28 (2) (2000) 408–428.
- [30] Z.I. Botev, Nonparametric density estimation via diffusion mixing, tech. rep., The University of Queensland, 2007. <<http://espace.library.uq.edu.au/view/UQ:120006>>.
- [31] M. Jones, I. McKay, T. Hu, Variable location and scale kernel density estimation, *Ann. Inst. Statist. Math.* 46 (3) (1994) 521–535.
- [32] S. Lee, C. Cho, J. Kim, S. Park, S. Yi, J. Kim, D. Cho, The effects of post-deposition processes on polysilicon Young's modulus, *J. Micromech. Microeng.* 8 (1998) 330.
- [33] H. Niederreiter, Quasi-Monte Carlo methods and pseudo-random numbers, *Am. Math. Soc.* 84 (6) (1978) 957.
- [34] D. Xiu, Efficient collocational approach for parametric uncertainty analysis, *Commun. Comput. Phys.* 2 (2) (2007) 293–309.
- [35] V. Barthelmann, E. Novak, K. Ritter, High dimensional polynomial interpolation on sparse grids, *Adv. Comput. Math.* 12 (4) (2000) 273–288.
- [36] S. Smolyak, Quadrature and interpolation formulas for tensor products of certain classes of functions, *Sov. Math. Dokl.* 4 (1963) 240–243.
- [37] C. O'Mahony, R. Duane, M. Hill, A. Mathewson, Electromechanical modeling of low-voltage RF MEMS switches, in: *Proc. IEEE – DTIP*, 2004, pp. 2–84813.
- [38] J. Marshall, D. Herman, P. Vernier, D. DeVoe, M. Gaitan, Young's modulus measurements in standard IC CMOS processes using MEMS test structures, *Electron Dev. Lett. IEEE* 28 (11) (2007) 960–963.